Nano Research 2014, 7(5): 794–803
DOI 10.1007/s12274-014-0440-0
Research Article

ISSN 1998-0124
CN 11-5974/O4

Mesocrystal Co_3O_4 nanoplatelets as high capacity anode materials for Li-ion batteries

Dawei Su[1,2], Shixue Dou[1] (✉), and Guoxiu Wang[2] (✉)

[1] *Institute for Superconducting & Electronic Materials, University of Wollongong, Wollongong, NSW 2522, Australia*
[2] *Centre for Clean Energy Technology, School of Chemistry and Forensic Science, University of Technology Sydney, Broadway, Sydney, NSW 2007, Australia*

Received: 3 January 2014
Revised: 25 February 2014
Accepted: 1 March 2014

KEYWORDS
msoporous material,
faceted crystal,
anode material,
lithium ion battery

ABSTRACT

Faceted crystals with exposed highly reactive planes have attracted intensive investigations for applications. Herein, we demonstrate a general synthetic method to prepare mesocrystal Co_3O_4 with predominantly exposed {111} reactive facets by the *in situ* thermal decomposition from $Co(OH)_2$ nanoplatelets. The mesocrystal feature was identified by field emission scanning electron microscopy, transmission electron microscopy, selected area electron diffraction, and N_2 isotherm analyses. When applied as anode material in lithium-ion batteries, mesocrystal Co_3O_4 nanoplatelets delivered a high specific capacity and an outstanding high rate performance. The superior electrochemical performance should be ascribed to the predominantly exposed {111} active facets and highly accessible surfaces. This synthetic strategy could be extended to prepare other mesocrystal functional nanomaterials.

1 Introduction

Mesoporosity provides highly accessible surfaces for many different applications in nanotechnology [1–3], such as fuel cells [4, 5], catalysts [6, 7], and electric energy storage [8–10]. Porous materials are usually prepared by the template nanocasting method, which involves either hard templates, such as porous alumina membranes [11, 12], carbon nanotubes [13], and porous silica [14–16], or soft templates (surfactants) [17–20]. The template-directed synthesis suffers from the disadvantages of low yield and high cost. Furthermore, the materials obtained by templating synthesis are polycrystalline, which cannot preserve long-range electronic connectivity and structural coherence. The specific facets of the nanomaterials are also crucial for technological applications. For example, the high energy {001} facet of anatase titanium oxide (TiO_2) demonstrated excellent photocatalytic activities [2], and high-index {311} facets of Cu_2O microcrystals showed an enhanced catalytic activity toward CO oxidation [21]. Shen's group reported low temperature oxidation of CO catalysed by faceted Co_3O_4 nanorods with a high percentage of exposed {110} planes [22]. Mesoporous Co_3O_4 with exposed active {110} facets possesses an outstanding capability for low

Address correspondence to Shixue Dou, shi@uow.edu.au; Guoxiu Wang, Guoxiu.Wang@uts.edu.au

temperature oxidation of trace ethylene [23]. Co_3O_4 with different morphologies were also reported for supercapacitor and lithium-ion batteries [24–31]. For energy storage applications, the specific facets are also important. Mesoporous NiO crystals with highly reactive exposed {110} facets demonstrated ultrafast lithium storage capability and high energy density [10]. This kind of material is called a "mesocrystal", as it contains a porous assembly of nanoscale crystallites with common orientation but no single coherent atomic domain [32, 33]. Recently, Crossland et al. [3] reported a general synthetic method for growing semiconductor mesocrystal of anatase TiO_2, based on seeded nucleation and growth inside a mesoporous template immersed in a dilute reaction solution.

Herein, we report a method to prepare mesocrystal Co_3O_4 by thermal decomposition of $Co(OH)_2$ precursor, following a formation mechanism that depends on low crystal mismatch between the precursor and the final product. When applied as electrode materials for Li-ion batteries, mesocrystal Co_3O_4 showed outstanding electrochemical performances. This general strategy could also be applicable to the synthesis of other mesoporous nanocrystals.

2 Materials and methods

2.1 Synthesis

$Co(OH)_2$ was first prepared as the precursor by a precipitation and hydrothermal process. In a typical procedure, 1.2 g of $Co(NO_3)_2{\cdot}6H_2O$ (Sigma-Aldrich, 98 wt.%) was dissolved in a 10 mL mixture of ethanol and distilled water with a 1:1 volume ratio. 1 g of poly(vinylpyrrolidone) (PVP, Sigma-Aldrich, average mol wt. 40,000) was added as surfactant. After 30 min magnetic stirring, 25 mL 0.4 M NaOH (Sigma-Aldrich, ⩾99.8%) aqueous solution was slowly added for over 1.5 h, which was accompanied by colour evolution from blue to red-pink, indicating the phase change from the α to β phase of $Co(OH)_2$. Then, the reaction suspension was quickly transferred into a Teflon-lined autoclave. The autoclave was heated to 120 ℃ and maintained at that temperature for 10 h. After cooling to room temperature, the pink product was collected by centrifugation and washed thoroughly with distilled water several times. The β-$Co(OH)_2$ precursor was obtained after drying for 12 h at 60 ℃ in a vacuum oven. The final mesoporous Co_3O_4 nanocrystals were prepared by annealing the β-$Co(OH)_2$ precursor at 450 ℃ for 2 h in a tube furnace in air with a slow heating rate (2.0 ℃·min^{-1}).

2.2 Structural and physical characterization

The phase and crystallographic structure of the Co_3O_4 materials were characterized by powder X-ray diffraction (XRD) using a Siemens D5000 diffractometer with Cu Kα1 radiation (λ = 1.54056 Å), with 2θ ranging from 10° to 90° and a scanning step of 0.02 (°)·s^{-1}. The morphology was analysed by high resolution field emission scanning electron microscopy (FESEM, Zeiss Supra 55VP). The microscope was operated at a working distance of 2 mm with an acceleration voltage of 10 kV, and an in-lens detector was used for imaging. The details of the crystal structure were further analysed by high-resolution transmission electron microscopy (HRTEM, FEGTEM 3000 JEOL 300 KV Atomic Resolution Transmission Electron Microscope with 0.192 nm resolution), conducted at an accelerating voltage of 300 kV. The bright field (BF) images and selected area electron diffraction (SAED) patterns were recorded by a Gatan charge-coupled device (CCD) camera in a digital format. The N_2 adsorption/desorption isotherms of materials were measured by a Micromeritics 3 Flex Surface Characterisation Analyser at 77 K. Brunauer–Emmett–Teller (BET) surface areas were calculated using experimental points at a relative pressure of P/P_0 = 0.05–0.25. The pore size distribution was calculated by the Barrett–Joyner–Halenda (BJH) method.

2.3 Electrochemical testing

The electrodes were prepared by dispersing the as-prepared Co_3O_4 particles (70 wt.%), acetylene carbon black (20 wt.%), and poly(vinylidene fluoride) binder (PVDF, 10 wt.%) in N-methyl-2-pyrrolidone (NMP, Sigma-Aldrich, 99.5%) to form a slurry. The resultant slurry was pasted onto copper foil using a doctor blade and dried at 100 ℃ for 12 h under vacuum, followed by pressing at 200 kg·cm^{-2}. Electrochemical measurements were carried out using two-electrode

coin cells with lithium metal as the counter electrode. The CR2032-type coin cells were assembled in an argon-filled glove box (UniLab, Mbraun, Germany). The electrolyte solution was 1 M $LiPF_6$ dissolved in a mixture of ethylene carbonate (EC) and dimethyl carbonate (DMC), with a volume ratio of 1:1. Cyclic voltammetry (CV) was carried out on a CHI 660C electrochemistry workstation with a scan rate of 0.1 $mV \cdot s^{-1}$ from 0.01 to 3.0 V in a two-electrode system. The charge–discharge measurements were performed at ambient temperature at different current densities in the voltage range from 0.01 to 3.0 V. In order to investigate the morphological changes of electrode, Swagelok-type cell was assembled. After cycling, the cell was disassembled in the glove before being used for *ex situ* SEM analysis.

3 Results and discussion

3.1 Phase, morphology, and structure characterization

We used a two-step method to obtain the Co_3O_4 nanoplatelets with predominantly exposed {111} facets, following a formation mechanism that depends on the low crystal mismatch between the precursor and final product. In the first step, the precursor was synthesized, in which the exposed facets have a similar arrangement of atoms to that of the targeted product Co_3O_4. In the second step, the precursor was converted to the final product after recrystallization and oxidization [34]. The $Co(OH)_2$ nanoplatelets with hexagonal shape were synthesised with the assistance of poly(vinylpyrrolidone) (PVP) surfactant (as shown in Fig. 1). All crystals have a uniform size distribution in the range of 200–300 nm and are less than 20 nm in thickness (Fig. S1 in the Electronic Supplementary Material (ESM)). The phase was identified by XRD (Fig. 2) and refined by the Rietveld method. The refined diffraction pattern confirms that the as-prepared hexagonal $Co(OH)_2$ crystals have triclinic symmetry with the $P\bar{3}m1$ space group (JCPDS No. 164). The lattice parameters were calculated as: $a = b = 3.1813$ Å, $c = 4.6481$ Å, and $\alpha = \beta = 90°$, $\gamma = 120°$, with satisfactory convergence factors $\chi^2 = 8.5$, $R_{wp} = 7.69\%$, $R_p = 13.04\%$.

The crystallographic structural features of the $Co(OH)_2$ were further characterized by TEM and

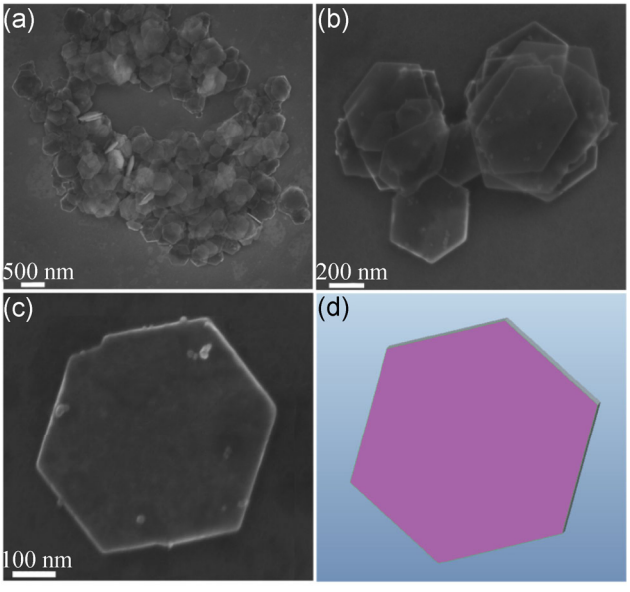

Figure 1 (a)–(c) FESEM images of hexagonal $Co(OH)_2$ at different magnifications; (d) The geometrical model corresponding to (c).

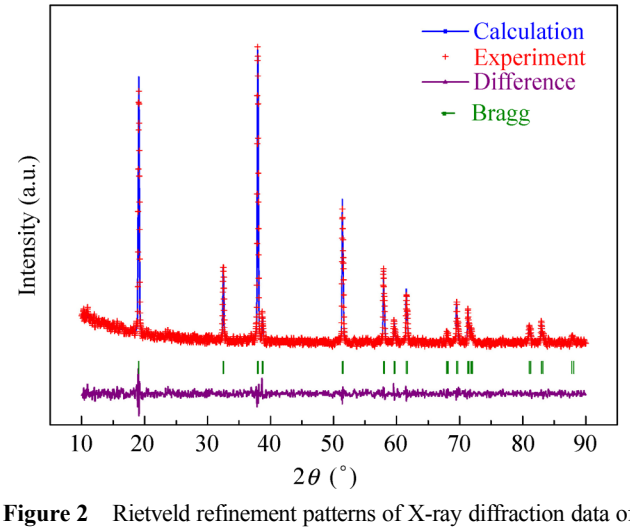

Figure 2 Rietveld refinement patterns of X-ray diffraction data of as-prepared $Co(OH)_2$, where the observed and calculated intensities are represented by red crosses and the blue solid line, respectively. The bottom purple line shows the fitting residual difference. Bragg positions are represented as light green ticks.

SAED (Fig. 3). A free-standing $Co(OH)_2$ crystal is thin enough to be transparent under the electron beam, as shown in the HRTEM images (Fig. 3(a)). The SAED pattern of individual $Co(OH)_2$ crystals (Fig. 3(b)) shows a perfect rhombus of spots, which can be well indexed along the [001] zone axis of hexagonal $Co(OH)_2$ (including the (100), $(1\bar{1}0)$, and $(0\bar{1}0)$ crystal planes), indicating single crystallinity. The lattice

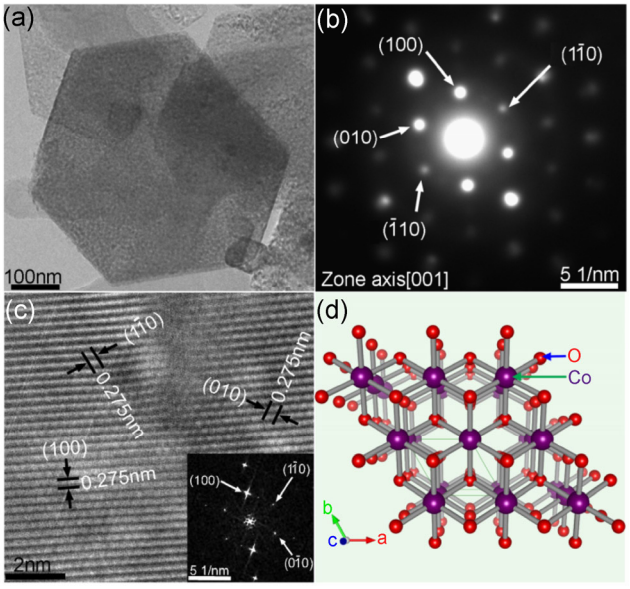

Figure 3 (a) TEM image of typical free standing hexagonal $Co(OH)_2$ nanoplatelets with perfect hexagonal sharp edges and corners, and well-defined faces. (b) SAED pattern taken from single nanoplatelet in (a), showing a perfect rhombus of diffraction spots along the [001] zone axis of hexagonal $Co(OH)_2$. (c) Lattice resolved HRTEM image recorded from (a). Inset of (c) is its corresponding indexed FFT pattern. (d) Crystal structure of $Co(OH)_2$ seen along the [001] direction.

resolved HRTEM image presented in Fig. 3(c) illustrates the interplanar distances of the (100), (1$\bar{1}$0), and (010) crystal planes (all are 0.275 nm) and the interfacial angles of 60° between them. The inset in Fig. 3(c) shows the corresponding fast-Fourier-transform (FFT) pattern, which can be fully indexed to the [001] zone axis of hexagonal $Co(OH)_2$. This confirms that the as-prepared $Co(OH)_2$ crystals have predominantly exposed {001} crystal planes (as illustrated in Fig. 3(d)).

After thermal decomposition, the obtained Co_3O_4 preserved the hexagonal nanoplatelet shape, as shown in the FESEM images (Figs. 4(a) and 4(b)). The nanoplatelets are also highly uniform, with a similar size distribution to the $Co(OH)_2$ precursor (Fig. S2 in the ESM). The surfaces of the Co_3O_4 crystals become much rougher than those of the $Co(OH)_2$ precursor, suggesting the generation of a porous structure. The individual Co_3O_4 nanoplatelet shown in Fig. 4(b) clearly presents the porous architecture. The phase of the Co_3O_4 was confirmed by XRD (Fig. 4(c)). All diffraction peaks can be indexed to the face-centred cubic phase with space group $Fd\bar{3}m$ (No. 227). The

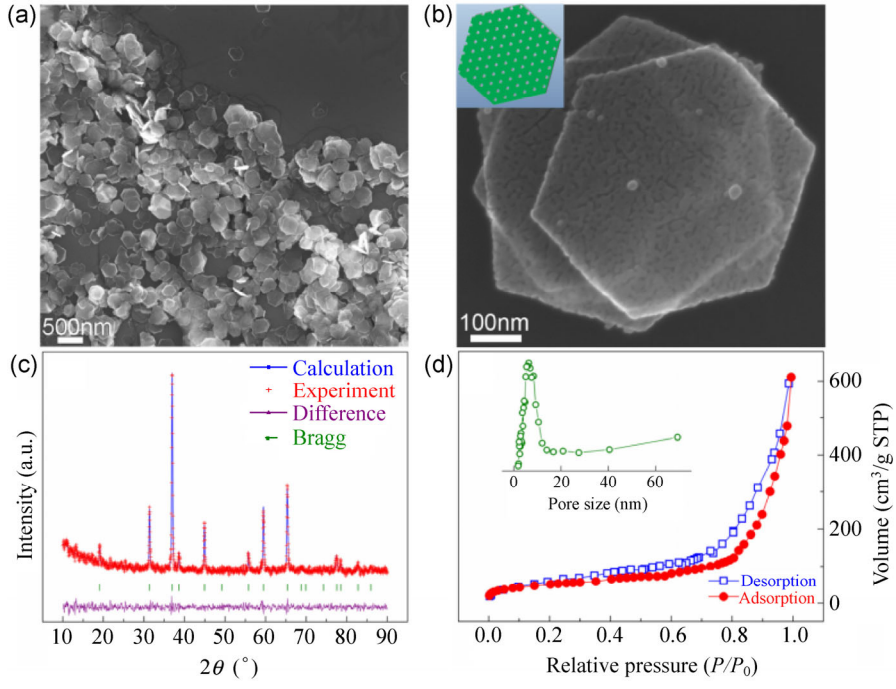

Figure 4 (a) Low and (b) high magnification FESEM images of hexagonal Co_3O_4. Inset of (b) is the corresponding geometrical model. (c) Rietveld refinement patterns of X-ray diffraction data of as-prepared Co_3O_4 crystals. The observed and calculated intensities are represented by red crosses and the blue solid line, respectively. The bottom purple line shows the fitting residual difference. Bragg positions are represented as light green ticks. (d) N_2 absorption/desorption isotherms of Co_3O_4 nanoplatelets; the inset is the corresponding pore size distribution of the Co_3O_4 nanoplatelets derived from absorption hysteresis of the BET surface area measurements.

lattice parameters were calculated to be $a = b = c =$ 8.085 Å, and $\alpha = \beta = \gamma = 90°$ ($\chi^2 = 8.62$, $R_{wp} = 7.98\%$, $R_p =$ 13.24%). No impurity phase was observed. Therefore, the $Co(OH)_2$ precursor has been transformed to porous Co_3O_4 by thermal decomposition treatment. The BET surface area and porosity were investigated by nitrogen adsorption/desorption isotherms at 77 K (as shown in Fig. 4(d)). The hysteresis feature can be classified as a typical type-IV isotherm with an H_1-type loop, reflecting the mesoporous nature of the Co_3O_4 crystals. The pore size distribution curve is shown as the inset in Fig. 4(d), which exhibits a monomodal pore size distribution with a mean pore size of 6.30 nm (calculated by the Barrett–Joyner–Halenda (BJH) method). The specific BET surface area was determined to be 79.3 $m^2 \cdot g^{-1}$.

The detailed crystallographic structural features of Co_3O_4 were further characterized by TEM and SAED (Fig. 5). Apparently, the targeted product (Co_3O_4) has maintained the hexagonal platelet shape and has mesoporous architecture (as shown in Fig. 5(a)). In the HRTEM image (Fig. 5(b)), the porosity features are easily observed. Remarkably, even though a porous structure is generated, the Co_3O_4 nanoplatelets are still single crystalline, which is compatible with the reported mesocrystal feature [35]. This is evidenced by the SAED spot pattern taken from an entire free-standing Co_3O_4 nanoplatelet (as shown in Fig. 5(c)). All the diffraction spots can be well indexed as $(0\bar{2}2)$, $(20\bar{2})$, and $(2\bar{2}0)$ crystal planes along the [111] zone axis of spinel Co_3O_4. The lattice resolution HRTEM image (Fig. 5(d)) shows the $(0\bar{2}2)$, $(20\bar{2})$, and $(2\bar{2}0)$ crystal planes with 0.28 nm lattice spacing and 60° interfacial angles between them. The corresponding FFT pattern (inset in Fig. 5(d)) can also be well indexed along the [111] crystal orientation of spinel Co_3O_4. This clearly confirms that the as-prepared mesoporous Co_3O_4 nanoplatelets have predominantly exposed {111} facets. The formation mechanism of the single-crystalline Co_3O_4 mesoporous nanoplatelets can be ascribed to the fact that the crystal mismatch is below 2% between the $Co(OH)_2$ {001} facets and the Co_3O_4 {111} facets. As demonstrated in Fig. 5(e), the difference in the lattice spacing between the $Co(OH)_2$ (100), $(1\bar{1}0)$, and $(0\bar{1}0)$ crystal planes, and the Co_3O_4 $(0\bar{2}2)$, $(20\bar{2})$, and $(2\bar{2}0)$ crystal planes, respectively, is less than 2%. Moreover, the interfacial angles between these planes are the same (60°). The rhombic atomic arrangement on the {111} surfaces is illustrated by 4 simulated formula units of the spinel Co_3O_4 crystal structure along the (111) projected direction (as shown in Fig. 6). Therefore, mesocrystal Co_3O_4 nanoplatelets with exposed {111} crystal planes have been successfully prepared.

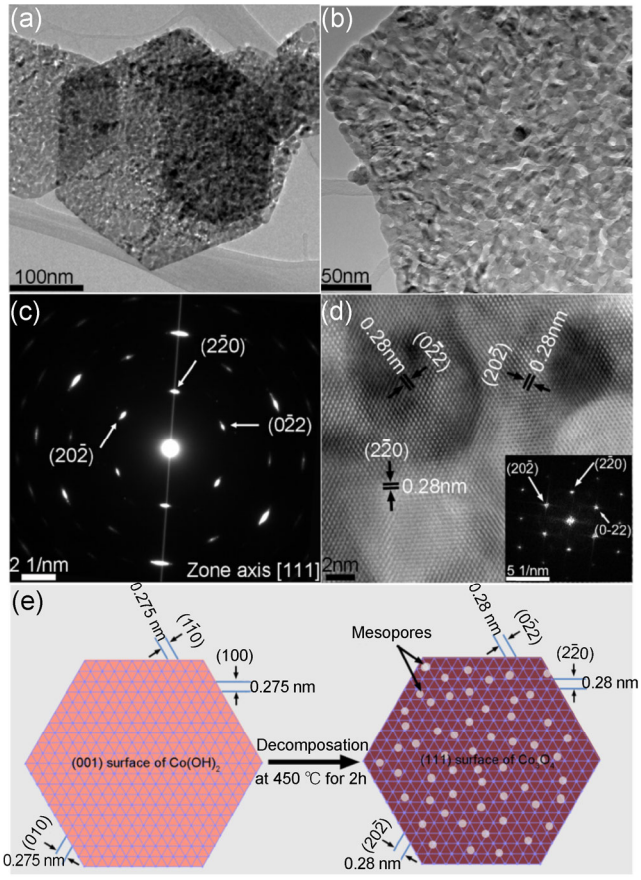

Figure 5 (a) TEM image of typical free standing hexagonal Co_3O_4 nanoplatelets with perfect hexagonal sharp edges and corners, and well-defined faces. (b) HRTEM image of a free-standing hexagonal Co_3O_4 nanoplatelet, showing the mesoporous structure. (c) SAED pattern taken from single nanoplatelet in (a), showing a perfect rhombus of diffraction spots along the [111] zone axis of spinel Co_3O_4. (d) Lattice resolution HRTEM image recorded from (a). Inset of (d) is its corresponding indexed FFT pattern. (e) Schematic diagram to introduce the mechanism through which the hexagonal $Co(OH)_2$ nanoplatelets are converted into Co_3O_4 nanoplatelets, while maintaining the single crystallinity because the crystal mismatch between $Co(OH)_2$ and Co_3O_4 is below 2%.

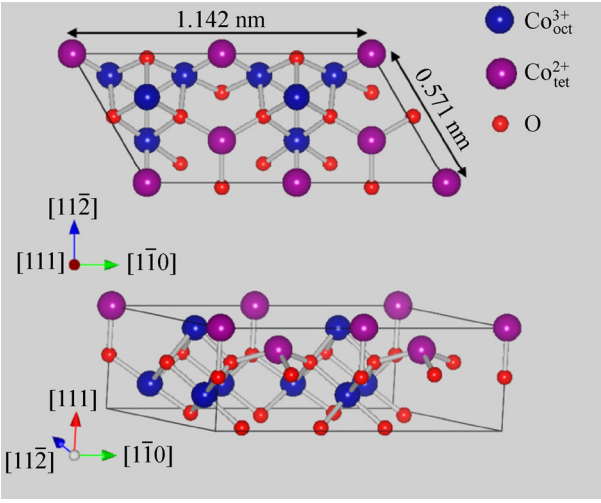

Figure 6 Top and lateral views of the atomic configuration of the {111} crystal planes based on 4 formula units ($4Co^{2+}8Co^{3+}16O$, 28 atoms in total). In the normal-spinel structure, Co_3O_4 has two kinds of Co ions: Co^{2+} and Co^{3+}. The former occupies one-eighth of the tetrahedral interstices, while the Co^{3+} ions occupy half of the octahedral interstices.

3.2 Electrochemical performance as anode material for Li-ion batteries

The electrochemical properties were studied by cyclic voltammetry (CV) and galvanostatic charge–discharge testing. The CV curves are shown in Fig. 7(a), in which one redox couple in the initial cycle presents at around 0.86 and 2.08 V in the cathodic and anodic processes, respectively. These peaks should correspond to the reversible reaction between Li^+ ions and Co_3O_4 [36], which are related to reduction of Co_3O_4 to Co, and the oxidation of the reduced Co to Co^{n+}: $8Li^+ + Co_3O_4 + 8e^- \leftrightarrow 3Co + 4Li_2O$ [37, 38]. The other broad peak in the lower discharge voltage range (~0.67 V) should be ascribed to the generation of solid electrolyte interphase (SEI) [36, 37]. According to previous research, the SEI formed on the surface of the electrodes contains an inorganic layer and an organic layer around the particles [39, 40]. The organic SEI layer can be formed and dissolved reversibly, which could contribute to the reversible capacity during the cycling processes. On the contrary, the generation of the inorganic SEI layer is an irreversible process, which will result in the irreversible capacity. In the subsequent cycles, cathodic peaks are positively shifted to 1.13 V, which is caused by polarisation of the electrode material. The overlapping CV curves in the 2nd and 3rd cycles

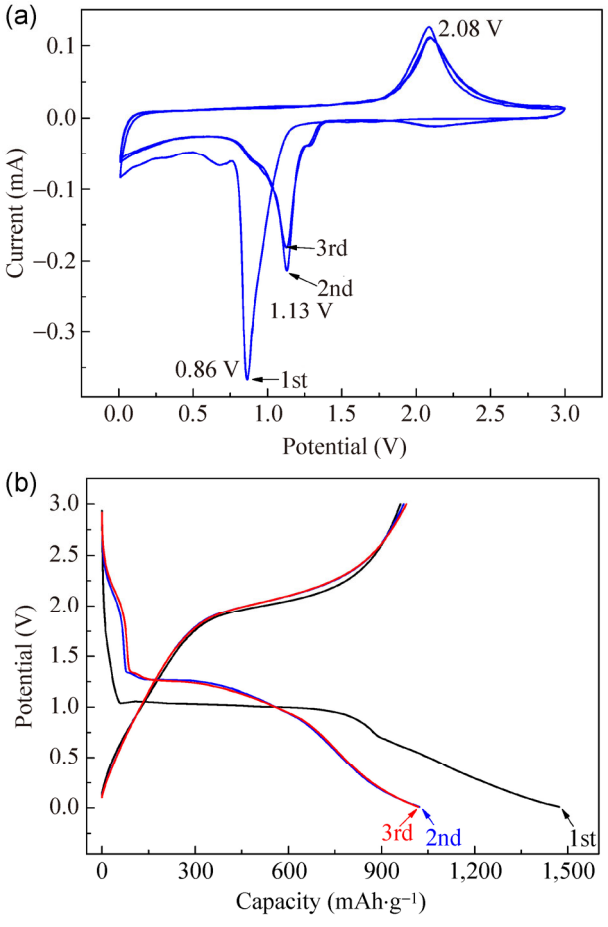

Figure 7 (a) CV curves for the first 3 cycles of the mesocrystal Co_3O_4 nanoplatelets as anode for the lithium ion cell. (b) Discharge and charge profiles for the first 3 cycles of mesocrystal Co_3O_4 nanoplatelets at the 0.5 C current rate.

indicate the promising stability of mesocrystal Co_3O_4 nanoplatelets. The CV measurements clearly illustrate the reversible lithium storage capability of the mesocrystal Co_3O_4 nanoplatelets.

The specific capacity of the mesocrystal Co_3O_4 nanoplatelets was tested by galvanostatic charge and discharge cycling. Figure 7(b) shows the charge and discharge profiles for the first 3 cycles at the 0.5 C rate. In the first cycle, the electrode delivered a discharge capacity of 1,480 mAh·g^{-1}, in which some of this capacity could be consumed in the formation of the SEI, including the irreversible inorganic SEI layer and the reversible organic SEI layer [41–43]. From the second cycle, the electrode maintained high reversibility and achieved a discharge capacity of about 1,020 mAh·g^{-1}.

Figure 8(a) shows the cycling performances of the as-prepared mesocrystal Co_3O_4 nanoplatelets at various current rates. It shows that mesocrystal Co_3O_4 nanoplatelets deliver high initial discharge capacities at different current rates: 1,492, 1,480, 1,349, 1,315, and 1,278 mAh·g^{-1} at 0.2 C, 0.5 C, 1 C, 5 C, and 10 C, respectively. Although the capacities decrease in the second cycle, the electrodes still maintained high capacities after 100 cycles: 1,160, 1,020, 995, 820, and 556 mAh·g^{-1} at 0.2 C, 0.5 C, 1 C, 5 C, and 10 C, respectively. Furthermore, the mesocrystal Co_3O_4 not only can retain high capacity at low current rates, but also demonstrated well-defined cycling performances at high current rates of 1 C, 5 C, and 10 C. At low current rates, the electrode achieved 95.8% and 99.8% capacity retention ratios (relative to second cycle capacities) after 100 cycles at 0.2 and 0.5 C, respectively. At high current rates such as 1 C and 10 C, the mesocrystal Co_3O_4 nanoplatelets exhibited 98.8% and 98.6% retention ratios (relative to the second cycle capacities) after 100 cycles, respectively [38, 43].

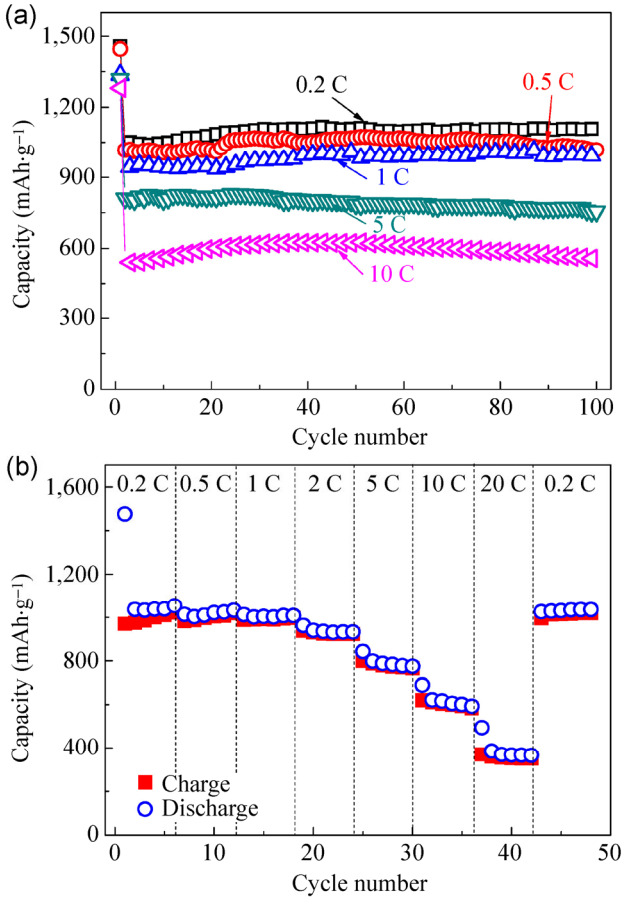

Figure 8 (a) Cycling performance of mesocrystal Co_3O_4 nanoplatelets at various current rates. (b) Rate performance of mesocrystal Co_3O_4 nanoplatelets at various current rates.

Figure 8(b) shows the cycling performance of the mesocrystal Co_3O_4 nanoplatelets at varied current rates. When the current rate is reversed back to the initial low current rate, the cell capacity recovers to the original values, indicating that the integrity of the mesocrystal Co_3O_4 nanoplatelets has been preserved, even after high rate cycling. This implies that Co_3O_4 nanoplatelets are tolerant to varying charge and discharge currents, which is preferred for high power applications.

In order to identify the morphology change of the mesocrystal Co_3O_4 nanoplatelets after cycling, we carried out *ex situ* SEM analyses on the electrode after 50 cycles. As shown in Fig. S3, the overall mesocrystal nanoplateletes shape has been retained. This indicates that the mesocrystal nanoplatelete architecture can sustain long term cycling.

The mesocrystal Co_3O_4 nanoplatelets exhibited much better electrochemical performance than the mesoporous polycrystalline Co_3O_4 prepared by the SBA-15 SiO_2 hard template method (Fig. S4 in the ESM). Although the SBA-15 mesoporous Co_3O_4 has a high surface area (90.4 m^2·g^{-1}), as shown in Fig. S5, it features non-competitive capacity and cyclability under the same testing conditions (Fig. S6 in the ESM). Therefore, the good electrochemical performance not only originates from the mesporous architecture, but also should be ascribed to the unique exposed crystal planes. Normally, Co_3O_4 is enclosed by low-indexed facets, such as {100} [44–46] or {110} [22], while the mesocrystal Co_3O_4 presents a highly active surface due to the predominantly exposed (111) crystal planes [47]. Generally, high-energy surfaces have a large density of low-coordinated atoms situated on steps and kinks, with high reactivity [48]. This favours fast ion transfer between the surface and the interior [49, 50]. Consequently, the {111} crystal planes provide reactive sites for reaction with lithium ions, which can facilitate a fast conversion reaction towards lithium during the charge and discharge processes. The superior transport kinetics of mesocrystal Co_3O_4 nanoplatelets is also confirmed by the a.c. impedance measurement (Fig. 9). It can be seen that both the

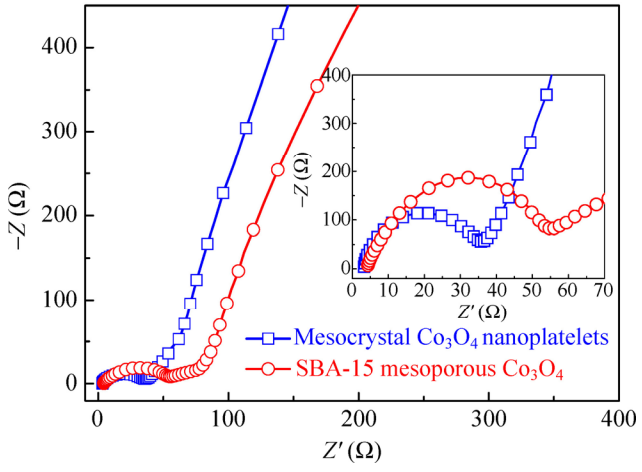

Figure 9 A.c. impedance spectra of mesocrystal Co_3O_4 nanoplatelets and SBA-15 mesoporous Co_3O_4. The inset is the magnified view in the high frequency range.

mesocrystal Co_3O_4 nanoplatelet and SBA-15 mesoporous Co_3O_4 electrodes show typical Nyquist plots, consisting of a single depressed semicircle in the high-medium frequency region and an inclined line at low frequency. The numerical value of the diameter of the semicircle on the Z' axis gives an approximate indication of the charge transfer resistance (R_{ct}). Apparently, the charge transfer impedance of the mesocrystal Co_3O_4 nanoplatelet electrode is much lower than that of the SBA-15 mesoporous Co_3O_4 electrode. The reduced charge transfer impedance is beneficial for the electrode kinetics, and consequently, improves the electrochemical performance.

Moreover, the mesoprous structure and the thinness (less than 20 nm) of the Co_3O_4 nanoplatelets can increase the contact area between the electrode and electrolyte, and allow easy penetration of the electrolyte and Li^+ ions, which all contribute to the excellent electrochemical performance.

4 Conclusions

We have demonstrated a facile approach to prepare mesocrystal Co_3O_4 nanoplatelets. TEM analysis revealed that the as-prepared mesocrystal Co_3O_4 nanoplatelets had predominantly exposed {111} crystal planes and mesoporous architecture. When applied as anode materials in lithium-ion cells, the mesocrystal Co_3O_4 delivered a higher reversible lithium storage capacity. After 100 cycles, the mesocrystal Co_3O_4 nanoplatelets retained lithium storage capacities of 983 and 750 $mAh \cdot g^{-1}$ at the 1 C and 5 C rate, respectively. Remarkably, this material also demonstrated an outstanding high rate performance, which mimics supercapacitors for high power delivery. The superior electrochemical performance could be ascribed to the predominantly exposed {111} reactive facets and the mesoporous nanostructure. Furthermore, the thin nanoplatelets also provide a short path for lithium transport. The concept of the mesocrystal architecture may be extended to other electrode materials for energy storage applications with high performances.

Acknowledgements

This original research was proudly supported by Commonwealth of Australia through the Automotive Australia 2020 Cooperative Research Centre (AutoCRC). The authors acknowledge use of facilities within the UOW Electron Microscopy Centre. The authors would like to also thank Dr. Tania Silver for critical reading.

Electronic Supplementary Material: Supplementary material (preparation details for 3-dimensional mesoporous Co_3O_4, FESEM images of $Co(OH)_2$, and Co_3O_4 nanoplatelets; FESEM, TEM, XRD and N_2 adsorption isotherms of 3-dimensional mesoporous Co_3O_4; electrochemical performance of 3-dimensional mesoporous Co_3O_4) is available in the online version of this article at http://dx.doi.org/10.1007/s12274-014-0440-0.

References

[1] Yuan, C. Z.; Xiong, S. L.; Zhang, X. G.; Shen, L. F.; Zhang, F.; Gao, B.; Su, L. H. Template-free synthesis of ordered mesoporous NiO/poly (sodium-4-styrene sulfonate) functionalized carbon nanotubes composite for electrochemical capacitors. *Nano Res.* **2009**, *2*, 722–732.

[2] Yang, H. G.; Sun, C. H.; Qiao, S. Z.; Zou, J.; Liu, G.; Smith, S. C.; Cheng, H. M.; Lu, G. Q. Anatase TiO_2 single crystals with a large percentage of reactive facets. *Nature* **2008**, *453*, 638–641.

[3] Crossland, E. J. W.; Noel, N.; Sivaram, V.; Leijtens, T.; Alexander-Webber, J. A.; Snaith, H. J. Mesoporous TiO_2 single crystals delivering enhanced mobility and optoelectronic device performance. *Nature* **2013**, *495*, 215–219.

[4] Bach, U.; Lupo, D.; Comte, P.; Moser, J. E.; Weissörtel, F.; Salbeck, J.; Spreitzer, H.; Grätzel, M. Solid-state dye-sensitized mesoporous TiO_2 solar cells with high photon-to-electron conversion efficiencies. *Nature* **1998**, *395*, 583–585.

[5] Mamak, M.; Coombs, N.; Ozin, G. Self-assembling solid oxide fuel cell materials: Mesoporous yttria-zirconia and metal-yttria-zirconia solid solutions. *J. Am. Chem. Soc.* **2000**, *122*, 8932–8939.

[6] Zhu, K.; Wang, D. H.; Liu, J. Self-assembled materials for catalysis. *Nano Res.* **2009**, *2*, 1–29.

[7] Zhang, Q.; Joo, J.-B.; Lu, Z. D.; Dahl, M.; Oliveira, D. Q. L.; Ye, M. M.; Yin, Y. D. Self-assembly and photocatalysis of mesoporous TiO_2 nanocrystal clusters. *Nano Res.* **2011**, *4*, 103–114.

[8] Li, Y. G.; Tan, B.; Wu, Y. Y. Mesoporous Co_3O_4 nanowire arrays for lithium ion batteries with high capacity and rate capability. *Nano Lett.* **2008**, *8*, 265–270.

[9] Su, D. W.; Kim, H. S.; Kim, W. S.; Wang, G. X. Mesoporous nickel oxide nanowires: Hydrothermal synthesis, characterisation and applications for lithium-ion batteries and supercapacitors with superior performance. *Chem. -Eur. J.* **2012**, *18*, 8224–8229.

[10] Su, D. W.; Ford, M.; Wang, G. X. Mesoporous NiO crystals with dominantly exposed {110} reactive facets for ultrafast lithium storage. *Sci. Rep.* **2012**, *2*, 924.

[11] Chen, J.; Xu, L. N.; Li, W. Y.; Gou, X. I. α-Fe_2O_3 nanotubes in gas sensor and lithium-ion battery applications. *Adv. Mater.* **2005**, *17*, 582–586.

[12] Xu, J. M.; Wang, A. Q.; Wang, X. D.; Su, D. S.; Zhang, T. Synthesis, characterization, and catalytic application of highly ordered mesoporous alumina-carbon nanocomposites. *Nano Res.* **2011**, *4*, 50–60.

[13] Sun, Z.; Yuan, H.; Liu, Z.; Han, B.; Zhang, X. A highly efficient chemical sensor material for H_2S: α-Fe_2O_3 nanotubes fabricated using carbon nanotube templates. *Adv. Mater.* **2005**, *17*, 2993–2997.

[14] Jiao, F.; Harrison, A.; Jumas, J.-C.; Chadwick, A. V.; Kockelmann, W.; Bruce, P. G. Ordered mesoporous Fe_2O_3 with crystalline walls. *J. Am. Chem. Soc.* **2006**, *128*, 5468–5474.

[15] Lee, I.; Zhang, Q.; Ge, J. P.; Yin, Y. D.; Zaera, F. Encapsulation of supported Pt nanoparticles with mesoporous silica for increased catalyst stability. *Nano Res.* **2011**, *4*, 115–123.

[16] Li, Q.; Yang, J. P.; Feng, D.; Wu, Z. X.; Wu, Q. L.; Park, S. S.; Ha, C.-S.; Zhao, D. Y. Facile synthesis of porous carbon nitride spheres with hierarchical three-dimensional mesostructures for CO_2 capture. *Nano Res.* **2010**, *3*, 632–642.

[17] Liu, L.; Kou, H.-Z.; Mo, W. L.; Liu, H. J.; Wang, Y. Q. Surfactant-assisted synthesis of α-Fe_2O_3 nanotubes and nanorods with shape-dependent magnetic properties. *J. Phys. Chem. B* **2006**, *110*, 15218–15223.

[18] Jia, C. J.; Sun, L. D.; Yan, Z. G.; You, L. P.; Luo, F.; Han, X. D.; Pang, Y. C.; Zhang, Z.; Yan, C. H. Single-crystalline iron oxide nanotubes. *Angew. Chem. Int. Ed.* **2005**, *117*, 4402–4407.

[19] Reitz, C.; Suchomski, C.; Weidmann, C.; Brezesinski, T. Block copolymer-templated $BiFeO_3$ nanoarchitectures composed of phase-pure crystallites intermingled with a continuous mesoporosity: Effective visible-light photocatalysts? *Nano Res.* **2011**, *4*, 414–424.

[20] Zhang, D. Q.; Li, G. S.; Yang, X. F.; Yu, J. C. A micrometer-size TiO_2 single-crystal photocatalyst with remarkable 80% level of reactive facets. *Chem. Commun.* **2009**, 4381–4383.

[21] Leng, M.; Liu, M. Z.; Zhang, Y. B.; Wang, Z. Q.; Yu, C.; Yang, X. G.; Zhang, H. J.; Wang, C. Polyhedral 50-facet Cu_2O microcrystals partially enclosed by {311} high-index planes: Synthesis and enhanced catalytic CO oxidation activity. *J. Am. Chem. Soc.* **2010**, *132*, 17084–17087.

[22] Xie, X. W.; Li, Y.; Liu, Z.-Q.; Haruta, M.; Shen, W. J. Low-temperature oxidation of CO catalysed by Co_3O_4 nanorods. *Nature* **2009**, *458*, 746–749.

[23] Hu, L. H.; Peng, Q.; Li, Y. D. Selective synthesis of Co_3O_4 nanocrystal with different shape and crystal plane effect on catalytic property for methane combustion. *J. Am. Chem. Soc.* **2008**, *130*, 16136–16137.

[24] Xiong, S. L.; Yuan, C. Z.; Zhang, X. G.; Xi, B. J.; Qian, Y. T. Controllable synthesis of mesoporous Co_3O_4 nanostructures with tunable morphology for application in supercapacitors. *Chem. -Eur. J.* **2009**, *15*, 5320–5326.

[25] Xiong, S. L.; Chen, J. S.; Lou, X. W.; Zeng, H. C. Mesoporous Co_3O_4 and CoO@C topotactically transformed from chrysanthemum-like $Co(CO_3)_{0.5}(OH)\cdot 0.11H_2O$ and their lithium-storage properties. *Adv. Funct. Mater.* **2012**, *22*, 861–871.

[26] Liu, D. Q.; Wang, X.; Wang, X. B.; Tian, W.; Bando, Y.; Golberg, D. Co_3O_4 nanocages with highly exposed {110} facets for high-performance lithium storage. *Sci. Rep.* **2013**, *3*, 2543.

[27] Xiao, Y.; Hu, C. W.; Cao, M. H. High lithium storage capacity and rate capability achieved by mesoporous Co_3O_4 hierarchical nanobundles. *J. Power Sources* **2014**, *247*, 49–56.

[28] Venugopal, N.; Lee, D.-J.; Lee, Y. J.; Sun, Y.-K. Self-assembled hollow mesoporous Co_3O_4 hybrid architectures: A facile synthesis and application in Li-ion batteries. *J. Mater. Chem. A* **2013**, *1*, 13164–13170.

[29] Xia, X. H.; Tu, J. P.; Xiang, J. Y.; Huang, X. H.; Wang, X. L.; Zhao, X. B. Hierarchical porous cobalt oxide array films prepared by electro-deposition through polystyrene sphere

template and their applications for lithium ion batteries. *J. Power Sources* **2010**, *195*, 2014–2022.

[30] Hu, L.; Yan, N.; Chen, Q. W.; Zhang, P.; Zhong, H.; Zheng, X. R.; Li, Y.; Hu, X. Y. Fabrication based on the Kirkendall effect of Co_3O_4 porous nanocages with extraordinarily high capacity for lithium storage. *Chem. -Eur. J.* **2012**, *18*, 8971–8977.

[31] Chen, J.; Xia, X.-H.; Tu, J.-P.; Xiong, Q.-Q.; Yu, Y.-X.; Wang, X.-L.; Gu, C.-D. Co_3O_4/C core/shell nanowire arrays as advanced materials for lithium ion batteries. *J. Mater. Chem.* **2012**, *22*, 15056–15061.

[32] Yue, W. B.; Xu, X. X.; Irvine, J. T. S.; Attidekou, P. S.; Liu, C.; He, H. Y.; Zhao, D. Y.; Zhou, W. Z. Mesoporous monocrystalline TiO_2 and its solid-state electrochemical properties. *Chem. Mater.* **2009**, *21*, 2540–2546.

[33] Bian, Z. F. ; Zhu, J.; Wen, J.; Cao, F. L; Huo, Y. N.; Qian, X. F.; Cao, Y.; Shen, M. Q.; Li, H. X.; Lu, Y. F. Single-crystal-like titania mesocages. *Angew. Chem. Int. Ed.* **2011**, *50*, 1105–1108.

[34] Li, L. S.; Sun, N. J.; Huang, Y. Y.; Qin, Y.; Zhao, N. N.; Gao, J. N.; Li, M. X.; Zhou, H. H.; Qi, L. M. Topotactic transformation of single-crystalline precursor discs into disc-like Bi_2S_3 nanorod networks. *Adv. Funct. Mater.* **2008**, *18*, 1194–1201.

[35] Wang, T. X.; Cölfen, H.; Antonietti, M. Nonclassical crystallization: Mesocrystals and morphology change of $CaCO_3$ crystals in the presence of a polyelectrolyte additive. *J. Am. Chem. Soc.* **2005**, *127*, 3246–3247.

[36] Poizot, P.; Laruelle, S.; Grugeon, S.; Dupont, L.; Tarascon, J.-M. Nano-sized transition-metal oxides as negative-electrode materials for lithium-ion batteries. *Nature* **2000**, *407*, 496–499.

[37] Barreca D.; Cruz-Yusta M.; Gasparotto A.; Maccato C.; Morales J.; Pozza A.; Sada C.; Sánchez L.; Tondello E. Cobalt oxide nanomaterials by vapor-phase synthesis for fast and reversible lithium storage. *J. Phys. Chem. C* **2010**, *114*, 10054–10060.

[38] Lou X. W.; Deng D.; Lee J. Y.; Archer L. A. Thermal formation of mesoporous single-crystal Co_3O_4 nano-needles and their lithium storage properties. *J. Mater. Chem.* **2008**, *18*, 4397–4401.

[39] Edström, K.; Gustafsson, T.; Thomas, J. O. The cathode-electrolyte interface in the Li-ion battery. *Electrochim. Acta* **2004**, *50*, 397–403.

[40] Poizot, P.; Laruelle, S.; Grugeon, S.; Tarascon, J.-M. Rationalization of the low-potential reactivity of 3d-metal-based inorganic compounds toward Li. *J. Electrochem. Soc.* **2002**, *149*, A1212–A1217.

[41] Balaya, P.; Li, H.; Kienle, L.; Maier, J. Fully reversible homogeneous and heterogeneous Li storage in RuO_2 with high capacity. *Adv. Funct. Mater.* **2003**, *13*, 621–625.

[42] Maier, J. Nanoionics: Ion transport and electrochemical storage in confined systems. *Nat. Mater.* **2005**, *4*, 805–815.

[43] Wang, G.; Liu, H.; Horvat, J.; Wang, B.; Qiao, S.; Park, J.; Ahn, H. Highly ordered mesoporous cobalt oxide nanostructures: Synthesis, characterisation, magnetic properties, and applications for electrochemical energy devices. *Chem. -Eur. J.* **2010**, *16*, 11020–11027.

[44] Feng, J.; Zeng, H. C. Size-controlled growth of Co_3O_4 nanocubes. *Chem. Mater.* **2003**, *15*, 2829–2835.

[45] Xu R.; Zeng, H. C. Mechanistic investigation on salt-mediated formation of free-standing Co_3O_4 nanocubes at 95 °C. *J. Phys. Chem. B* **2003**, *107*, 926–930.

[46] Varghese, B.; Zhang, Y. S.; Dai, L.; Tan, V. B. C.; Lim, C. T.; Sow, C.-H. Structure-mechanical property of individual cobalt oxide nanowires. *Nano Lett.* **2008**, *8*, 3226–3232.

[47] Zhou, Z.-Y.; Tian, N.; Li, J.-T.; Broadwell, I.; Sun, S.-G. Nanomaterials of high surface energy with exceptional properties in catalysis and energy storage. *Chem. Soc. Rev.* **2011**, *40*, 4167–4185.

[48] Lebedeva, N. P.; Koper, M. T. M.; Feliu, J. M.; van Santen, R. A. Role of crystalline defects in electrocatalysis: Mechanism and kinetics of co adlayer oxidation on stepped platinum electrodes. *J. Phys. Chem. B* **2002**, *106*, 12938–12947.

[49] Zhang, D. Q.; Wen, M. C.; Zhang, P.; Zhu, J.; Li, G. S.; Li, H. X. Microwave-induced synthesis of porous single-crystal-like TiO_2 with excellent lithium storage properties. *Langmuir* **2012**, *28*, 4543–4547.

[50] Chen, J. S.; Liu, H.; Qiao, S. Z.; Lou, X. W. Carbon-supported ultra-thin anatase TiO_2 nanosheets for fast reversible lithium storage. *J. Mater. Chem.* **2011**, *21*, 5687–5692.